processes

MDPI

Article

Investigating the Effect of Bi_2MoO_6/g-C_3N_4 Ratio on Photocatalytic Degradation of Sulfadiazine under Visible Light

Ke Li [1,2], Miaomiao Chen [1], Lei Chen [1,*], Songying Zhao [1], Wencong Xue [1] and Yanchao Han [2]

[1] Key Laboratory of Song Liao Aquatic Environment, Ministry of Education, Jilin Jianzhu University, Changchun 130118, China
[2] State Key Laboratory of Electroanalytical Chemistry, Changchun Institute of Applied Chemistry, Chinese Academy of Sciences, Changchun 130022, China
* Correspondence: chenlei.jliae@hotmail.com

Abstract: In this study, a series of Bi_2MoO_6/g-C_3N_4 composites were prepared through a wet-impregnation method, and their photocatalytic properties were investigated for the degradation of sulfadiazine (SDZ) under visible light irradiation. Physical and chemical characterizations were carried out using X-ray diffraction (XRD), scanning electron microscope (SEM), Fourier transform infrared spectroscopy (FT-IR), photoluminescence spectroscopy (PL), UV-vis diffuse reflectance spectra (UV-vis), and electrochemical impedance spectra (EIS). Compared to pure g-C_3N_4, the introduction of Bi_2MoO_6 significantly enhanced the visible light responsive photocatalytic activity, with the 1:32 Bi_2MoO_6/g-C_3N_4 composite exhibiting the highest photodegradation efficiency towards SDZ under visible light irradiation with a photocatalytic efficiency of 93.88% after 120 min of visible light irradiation. The improved photocatalytic activity can be attributed to the formation of a heterojunction between Bi_2MoO_6 and g-C_3N_4, which promotes the transfer of photogenerated electron-hole pairs, thereby elevating its photocatalytic activity. The results suggest that Bi_2MoO_6/g-C_3N_4 composites have potential application for the degradation of sulfonamides in aquatic environments.

Keywords: visible light; photocatalysis; Bi_2MoO_6/g-C_3N_4; sulfadiazine

Citation: Li, K.; Chen, M.; Chen, L.; Zhao, S.; Xue, W.; Han, Y. Investigating the Effect of Bi_2MoO_6/g-C_3N_4 Ratio on Photocatalytic Degradation of Sulfadiazine under Visible Light. *Processes* **2023**, *11*, 1059. https://doi.org/10.3390/pr11041059

Academic Editors: Zhaoyang Wang, Hao Xu, Yan Feng and Hikmat S. Hilal

Received: 27 February 2023
Revised: 23 March 2023
Accepted: 27 March 2023
Published: 31 March 2023

1. Introduction

Sulfonamides are a type of antibiotics commonly employed in both human and veterinary medicine as well as in the agricultural industry, to prevent and treat bacterial infections [1–3]. They work by competitively hindering the synthesis of folic acid, an essential nutrient for bacterial growth, through their structural resemblance to para-aminobenzoic acid in bacterial cells [4,5]. Although they have been found to be effective in treating infections, the widespread use of sulfonamides has led to serious environmental problems, particularly in the water environment. Sulfonamides are not easily degraded in the environment and can persist in water for prolonged periods of time [6,7]. They can reach aquatic environments through various pathways such as wastewater discharge from municipal wastewater treatment plants [8], agricultural runoff [9], and discharge from hospitals and other healthcare facilities [10,11]. Once in the water, sulfonamides cannot be efficiently removed by conventional wastewater treatment processes, which can lead to their accumulation in rivers, lakes, and estuaries [12–14]. Sulfonamides have been detected in surface and groundwaters worldwide, as well as in aquatic organisms [15–19]. Kokoszka et al. found sulfamethoxazole and sulfapyridine as the most frequently detected pollutants in surface waters, with maximum concentrations of 78.88 ng L^{-1} and 38.88 ng L^{-1}, respectively [16]. Qin et al. conducted a study on the presence and distribution of ten sulfonamides in various aquatic environments of the Huixian karst wetland system in Guilin, China. Their research found that sulfamethoxypyridazine, sulfadiazine, sulfamethoxazole, and sulfamethazine had the highest concentrations among the ten sulfonamides detected

and the study also revealed that the highest ecological risks were observed in ditch water, with sulfachloropyridazine posing the greatest risk, and human health risks were observed for sulfonamides in drinking groundwater [17]. In a long-term study in Lower Saxony, Spielmeyer et al. detected sulfamethazine in groundwater at concentrations up to 100 ng L^{-1}. Nine sulfonamides were applied to two soil types, with sulfamethazine and sulfamethoxazole frequently detected in water samples taken from below the soil, and their presence persisted even four years after the last application [20]. Once in the water, sulfonamides can be harmful to aquatic life, including fish, invertebrates, and microorganisms, due to their toxic effects at high concentrations [21]. These sulfonamides can interfere with the metabolism and growth of algae, which are vital primary producers in aquatic environments, leading to reduced oxygen levels and death of other aquatic organisms that rely on algae for their survival [22,23]. Moreover, sulfonamides can have toxic effects on fish and other aquatic animals, including impairing growth, reproduction, and immune function [24]. For example, Hu et al. investigated the effects of sulfamethoxazole on juvenile Nile tilapia and found that high concentrations (100 µg/L) of sulfamethoxazole increased oxidative damage and induced an inflammatory response, as evidenced by changes in enzyme activities and gene expression [25]. In addition to the toxic effects on aquatic life, the presence of sulfonamides in water can disrupt the balance of the ecosystem [21]. It can induce changes in species composition and the loss of biodiversity. Furthermore, sulfonamides can also contribute to the spread of antibiotic resistance genes (ARGs) in the environment. ARGs are genes that confer resistance to antibiotics and can be easily transferred from one bacterium to another. Gao's study measured antibiotics, ARGs, and bacteria in a wastewater treatment plant and found reduced ARGs and bacteria in effluent, although the *sulI* gene remained stable, while correlations were significant between resistant bacteria and antibiotic concentrations [26]. Sabri et al. conducted a study on a Dutch river that receives wastewater treatment plant effluent, analyzing the occurrence of antibiotics and antibiotic resistance genes. They found that the wastewater treatment plants significantly increased the amount of antibiotics and ARGs in the river, and while antibiotics decreased once in the river, ARGs persisted up to 20 km downstream. The study highlights the potential for rivers to act as a reservoir of ARGs, even in regions with low human antibiotic usage [27]. Once present in the environment, ARGs can persist for long periods of time, increasing the risk of the spread of antibiotic resistance. This is a major concern as these bacteria can pose a threat to human health, making it difficult to treat infections.

Various approaches have been developed to efficiently remove antibiotics from wastewater, with Advanced Oxidation Processes (AOPs) being one of the most effective techniques for reducing or treating persistent antibiotics in wastewater [21,28,29]. Fenton oxidation and ozonation are frequently utilized AOP techniques for removing antibiotics from wastewater [30,31]. Santos et al. conducted a study to evaluate the degradation of norfloxacin using direct photolysis, UV/H_2O_2, and Fenton's oxidation. The results indicated that UV/H_2O_2 and Fenton's oxidation were effective in removing norfloxacin, achieving degradation rates of 100% and 60% and mineralization rates of 32% and 55%, respectively [32]. Lakovides et al. found that ozonation of urban wastewater with specific hydraulic retention times and ozone doses completely removed eight antibiotics, while also effectively inactivating Escherichia coli and reducing abundance of antibiotic resistance genes [33]. However, the main drawback of these technologies is the high energy requirements and equipment costs associated with their implementation [31,34]. As a result, the high cost of these strategies may limit their practical application. To overcome this challenge, more economical and eco-friendly approaches are needed to effectively remove antibiotics from wastewater. Bio-electrochemical technology, which involves the integration of combined microbial electrolytic cells (MECs) and microbial fuel cells (MFCs) with electrochemical-redox and bacterial metabolism, has been reported as a promising method for antibiotic degradation through redox reaction processes [35]. Furthermore, photocatalysis is considered a superior approach to treat wastewater more efficiently and at less cost. Photocatalysis involves the

use of light and a photocatalyst to generate reactive species that degrade contaminants in the wastewater [36]. It is a green and sustainable process that does not require the addition of chemicals, making it more economical and environmentally friendly [37].

Photocatalysis is a process that employs a photocatalyst to absorb light energy and create reactive oxygen species, which can then react with both organic and inorganic contaminants in wastewater, leading to their degradation [38–40]. As such, the role of the photocatalyst in photocatalysis is crucial, as it serves as the catalyst for the reaction and determines the efficiency of the process [41]. The photocatalyst must possess specific properties, such as high surface area, good stability, and excellent light absorption, to maximize the photocatalytic activity [42,43]. Over the past few decades, significant research efforts have been focused on developing highly efficient photocatalysts to tackle the increasing pollution problem caused by organic contaminants. One of the most promising approaches is the use of photocatalysts to degrade organic pollutants. Over the past few decades, a wide range of photocatalysts, including TiO_2 [44], ZnO [45], Ag_3PO_4 [46], Fe_2O_3 [47], Bi_2O_3 [48], and WO_3 [49], have been explored for the photocatalytic degradation of various organic pollutants. Among them, graphitic carbon nitride (g-C_3N_4) is a promising visible-light-driven photocatalyst due to its high stability, non-toxicity, and low cost [50,51]. However, its photocatalytic activity is often limited by its low electron-hole separation efficiency and narrow absorption range [52]. To address these limitations, various strategies have been employed to improve the photocatalytic performance of g-C_3N_4-based composite photocatalysts. One approach is to introduce co-catalysts, such as metal oxides, to enhance the photocatalytic activity of g-C_3N_4. For instance, TiO_2 has been widely used as an effective co-catalyst due to its good photocatalytic activity and high chemical stability [53]. Jiang et al. synthesized a novel spherical TiO_2/g-C_3N_4 hybrid through solvothermal synthesis, characterized it by various techniques, and evaluated its photocatalytic activity in the degradation of Methyl Blue under visible light irradiation. The hybrid showed excellent photoactivity, with an optimum TiO_2/g-C_3N_4 mass ratio of 12:1 that was 12.5 times and 87.5 times higher than that of nanosheet TiO_2 and powder g-C_3N_4, respectively [54]. However, the wide bandgap of TiO_2, with a value of approximately 3.2 eV for the anatase phase, poses a significant challenge to its photoactivation by visible solar light photons with a wavelength greater than 360 nm [55]. Furthermore, the high recombination rate of photogenerated electron-hole pairs contributes to the low quantum yield of TiO_2, which further limits its efficacy for visible-light photocatalysis [56]. All these greatly limit its practical application in visible-light photocatalysis. Recently, bismuth molybdate (Bi_2MoO_6) has emerged as a promising photocatalyst for visible-light-driven photocatalysis due to its excellent optical absorption, high carrier mobility, and high redox potential. Bi_2MoO_6 has been reported to have superior photocatalytic performance in the degradation of various organic contaminants, including pharmaceuticals and personal care products. The photocatalytic activity of Bi_2MoO_6 can be attributed to the formation of a heterojunction with g-C_3N_4, which promotes the separation and migration of photogenerated charge carriers. The construction of a heterojunction between Bi_2MoO_6 and g-C_3N_4 can be achieved through various methods, including hydrothermal, solvothermal, and impregnation methods. Fu et al. synthesized a visible-light-driven 2D/2D Bi_2MoO_6/g-C_3N_4 photocatalyst using hydrothermal coprecipitation, which demonstrated 3.9 and 2.5 times higher degradation rates for the contaminant naproxen compared to g-C_3N_4 and Bi_2MoO_6, respectively [57]. Kasinathan et al. synthesized a 3D/2D Bi_2MoO_6/g-C_3N_4 composite photocatalyst using the solvothermal method and evaluated its photocatalytic activity in the degradation of dyes. The composite showed superior photocatalytic performance, enhanced stability, and reduced recombination rates, with both superoxide and hydroxyl radicals playing a predominant role in the photocatalytic reaction [58]. Among them, wet-impregnation is a simple and effective method to prepare Bi_2MoO_6/g-C_3N_4 composite photocatalysts, which can facilitate the uniform distribution of Bi_2MoO_6 on the surface of g-C_3N_4 and the formation of a heterojunction between Bi_2MoO_6 and g-C_3N_4.

The photocatalytic degradation of sulfadiazine (SDZ), a commonly used antibiotic, has been of great interest due to its persistence and potential health and environmental risks [59]. Despite its widespread use, the degradation of SDZ has been challenging due to its complex structure and high stability. Therefore, the development of an efficient and effective photocatalytic system to degrade SDZ is of great significance.

While previous studies have explored the photocatalytic properties of Bi_2MoO_6 and g-C_3N_4 composites for various pollutants, our work is the first to focus specifically on the degradation of sulfadiazine and the optimization of the composite ratio to achieve the highest photo-catalytic efficiency. In this study, we aim to provide a novel contribution to the field by systematically investigating the impact of different Bi_2MoO_6/g-C_3N_4 composite ratios on the photocatalytic degradation of sulfadiazine under visible light irradiation. Hence, we have synthesized a series of Bi_2MoO_6/g-C_3N_4 hybrid nanocomposites with different mass ratios of Bi_2MoO_6 to g-C_3N_4 using a wet-impregnation method. The physical and chemical properties of the as-prepared materials were characterized by various techniques such as X-ray diffraction (XRD), Fourier transform infrared spectroscopy (FT-IR), photoluminescence spectroscopy (PL), UV-vis diffuse reflectance spectra (UV-vis), and electrochemical impedance spectra (EIS). The photocatalytic performance of these materials was evaluated in the degradation of SDZ under visible light irradiation. This work introduces a simple and efficient method for preparing a photocatalyst to remove sulfonamides under visible light. With its promising results, it holds significant potential for application in wastewater treatment.

2. Materials and Methods

2.1. Materials

The urea, $Bi(NO_3)_3 \cdot 5H_2O$, sodium molybdate ($Na_2HPO_4 \cdot 12H_2O$) and sodium hydroxide (NaOH) used in this study were procured from Tianjin Xintong Fine Chemicals Company Limited, Tianjin, China, while the SDZ was obtained from Shanghai McLean Biochemical Technology Co., Ltd., Shanghai, China. All reagents utilized in this study were analytical grade and used without any further purification. The preparation of all solutions was carried out using deionized water.

2.2. Preparation of Photocatalyst

2.2.1. Synthesis g-C_3N_4

Ten g of urea, a white crystalline organic compound, were accurately weighed and placed in a covered crucible. The crucible containing the urea was heated at a temperature of 550 °C for a duration of 4 h, with a controlled heating rate of 2 °C per minute in a muffle furnace. The aim of this thermal treatment was to induce a solid-state polymerization reaction, leading to the formation of a yellow-colored powder. The resulting powder was collected and allowed to cool to room temperature. To ensure the purity of the product, the powder was subjected to a thorough washing process using deionized water and ethanol, and then dried at a temperature of 60 °C for a period of 12 h. After drying, the obtained powder was subjected to a calcination process at a temperature of 500 °C for a duration of 330 min, with a controlled heating rate of 5 °C per minute, in a muffle furnace. The resultant material was identified as g-C_3N_4.

2.2.2. Synthesis Bi_2MoO_6

To prepare Bi_2MoO_6, 0.97 g of $Bi(NO_3)_3 \cdot 5H_2O$ and 0.242 g of $Na_2MoO_4 \cdot 2H_2O$ were dissolved in 38 mL of deionized water. The resulting solution was stirred with a magnetic stirrer for 1 h and then subjected to 30 min of ultrasonication to ensure a homogeneous dispersion. The pH of the mixture was adjusted to 6 using a 2.0 mol/L NaOH solution, and the solution was stirred for an additional hour to achieve a uniform suspension. The mixture was then transferred to a hydrothermal reaction vessel and maintained at a temperature of 160 °C for 12 h. After completion of the hydrothermal reaction, the

resulting yellow solid was collected by filtration, and washed alternatively with ethanol and deionized water several times. Finally, the sample was dried at 60 °C for 24 h.

2.2.3. Synthesis Bi_2MoO_6/g-C_3N_4

The Bi_2MoO_6/g-C_3N_4 composite was synthesized by means of wet-impregnation. To be brief, 0.3 g g-C_3N_4 was first dispersed in 20 mL of methanol and sonicated for 1 h. Then, the Bi_2MoO_6 photocatalyst was added to the dispersion, and the mixture was subjected to sonication at room temperature for an additional hour. The resulting amalgam was then placed on a magnetic stirrer and stirred continuously for 24 h to ensure uniform loading of Bi_2MoO_6 onto the surface of g-C_3N_4. The resulting composite was separated by centrifugation, washed with deionized water and ethanol, and dried at 60 °C for 24 h. To investigate the effect of the mass ratio of Bi_2MoO_6 to g-C_3N_4 on the photocatalytic performance of the composite, composites were prepared with different ratios of Bi_2MoO_6 to g-C_3N_4, namely, 1:4 Bi_2MoO_6/g-C_3N_4, 1:8 Bi_2MoO_6/g-C_3N_4, 1:16 Bi_2MoO_6/g-C_3N_4, and 1:32 Bi_2MoO_6/g-C_3N_4.

2.3. Characterization

The XRD analysis was performed using a Rigaku UltimaIV X-ray diffractometer with Cu Kα radiation over the 2θ range of 10–90°. SEM images were obtained using an FEI Quanta-PEG 450 microscope. PL were obtained using a F-98 system (Shanghai, China), while the FT-IR spectrum was recorded using a PerkinElmer Spectrum Two spectrometer. UV-vis were obtained using a TU-1901 spectrophotometer with a wavelength range of 200–800 nm. EIS were recorded using an electrochemical workstation (Ivium Technologies BV, Ivium, Eindhoven, the Netherlands) with a standard three-electrode configuration consisting of a working electrode, a platinum plate as a counter electrode, and a standard Ag/AgCl reference electrode in saturated KCl solution. A 0.5 M Na_2SO_4 solution was employed as the electrolyte in this analysis.

2.4. Photocatalytic Experiments

The photocatalytic degradation of SDZ by Bi_2MoO_6/g-C_3N_4 samples was assessed under irradiation by a 500 W xenon lamp, incorporating a 420 nm cut-off filter. A solution of SDZ (3 mg/L) was prepared, to which 100 mg of the prepared photocatalysts was added, and the solution was subsequently diluted to a volume of 50 mL. To ensure an adsorption/desorption equilibrium between the SDZ and the photocatalysts, the suspensions were magnetically stirred for 30 min in the dark prior to irradiation. A 1.5 mL quantity of the suspension was extracted at regular intervals and subjected to filtration through a 0.22 μm filter (Millipore) for testing of the residual SDZ concentration. The concentration of SDZ was quantified by HPLC (Agilent Technologies 1200-Series). To evaluate the stability and reusability of the photocatalyst, cyclic experiments of SDZ photodegradation were performed. Subsequent to each operational cycle, the photocatalyst material was subjected to filtration through 0.22 μm polyether sulfone membranes, followed by thorough washing with deionized water in readiness for the ensuing cycle.

3. Results and Discussion

3.1. Characterization

The preparation of g-C_3N_4 which utilizes urea as the precursor, through thermal oxidative stripping, yields a significant amount of irregularly layered structures, as depicted in Figure 1a. This layered configuration facilitates the reduction of electron transfer pathways, thereby enhancing the migration of photocarriers, and results in an increase in both surface area and pore volume, providing a greater number of active sites. Figure 1b shows the pure Bi_2MoO_6, which exhibits a blocky, stacked morphology. The block-like structures are approximately 200–400 nm in size and exhibit a noticeable phenomenon of aggregation. Figure 1c depicts the Bi_2MoO_6/g-C_3N_4 composite photocatalyst, which has been prepared through wet-impregnation. It is evident that the blocky Bi_2MoO_6 structures

are dispersed on the surface of g-C_3N_4, and the aggregation of these block-like structures is diminished, primarily due to the role of g-C_3N_4 nanosheets as the substrate for Bi_2MoO_6. This observation confirms the successful loading of Bi_2MoO_6 onto layered g-C_3N_4, and the formation of a heterojunction between the blocky Bi_2MoO_6 and the g-C_3N_4 nanosheet surface, which promotes the transfer of photogenerated electron-hole pairs, thereby elevating its photocatalytic activity.

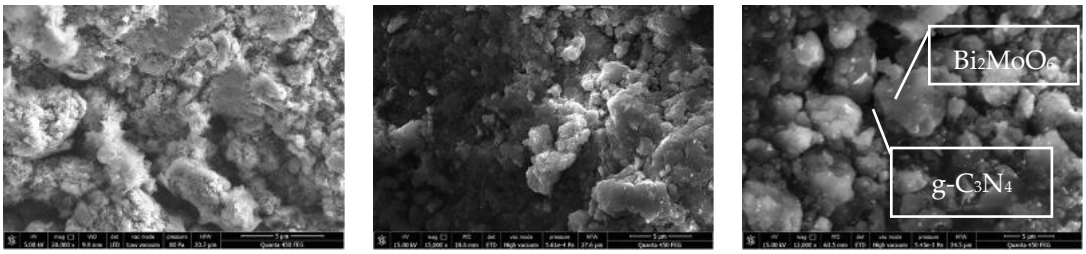

Figure 1. SEM images of (**a**) g-C_3N_4, (**b**) Bi_2MoO_6 and (**c**) 1:32 Bi_2MoO_6/g-C_3N_4.

The XRD analysis of g-C_3N_4, as depicted in Figure 2, reveals two distinct peaks in the vicinity of 2θ values of 13.0° and 27.4°. The peak located at approximately 13.0° corresponds to the (100) crystal plane of g-C_3N_4, while the peak located at approximately 27.4° corresponds to the (002) crystal plane. These peaks are in an agreement with the characteristic XRD spectrum of g-C_3N_4 (JCPDS 87-1526). In the case of Bi_2MoO_6, the XRD analysis reveals several distinct peaks at 2θ values of 27.361°, 31.705°, 32.562°, 45.481°, 53.905°, 56.441°, and 66.429 °which corresponded to the (131), (200), (151), (202), (331), (262), and (004) crystal planes, respectively, of orthorhombic Bi_2MoO_6 as per the standard card (JCPDS No.76-2388). The XRD analysis of the 1:32 Bi_2MoO_6/g-C_3N_4 composite reveals the characteristic peaks of both g-C_3N_4 and Bi_2MoO_6. The peaks of Bi_2MoO_6 (131), (200), (151), (202), (331), and (262) are particularly pronounced, and no other impurities were detected. This indicates that the 1:32 Bi_2MoO_6/g-C_3N_4 composite has been prepared successfully.

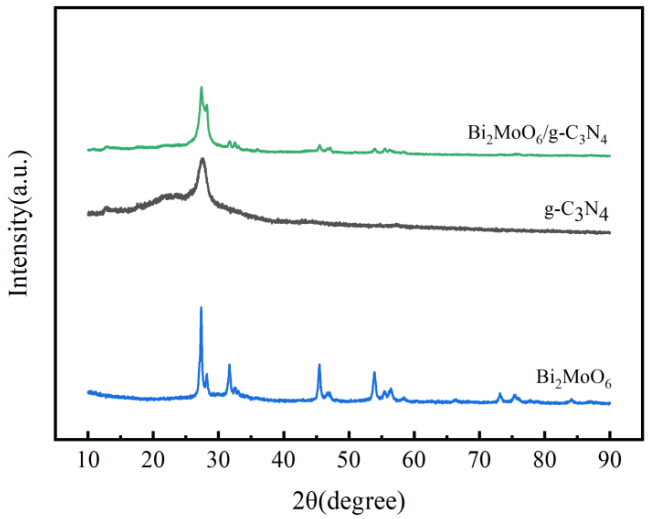

Figure 2. XRD pattens of g-C_3N_4, Bi_2MoO_6 and 1:32 Bi_2MoO_6/g-C_3N_4.

As shown in Figure 3, the FT-IR spectra of various ratios of Bi_2MoO_6/g-C_3N_4 composites display notable absorption peaks around 810 cm^{-1}, 1200–1700 cm^{-1}, and 3200–3400 cm^{-1}, which correspond to the absorption peaks of pure g-C_3N_4. The sharp absorption peak around 810 cm^{-1} corresponds to the bending vibration of the 3-s-triazine ring, while multiple absorption peaks between 1200–1700 cm^{-1} are attributed to the stretching and bending vibrations of C-N and C=N heterocycles. The broad absorption peak around

3200–3400 cm^{-1} may be attributed to the stretching vibrations of NH and NH_2 groups or the stretching vibrations of O-H in H_2O molecules, indicating that the composite process did not disrupt the structure of g-C_3N_4, which is consistent with the XRD characterization results. The range between 732–841 cm^{-1} is primarily due to the stretching vibrations of Mo-O, while the range between 450–565 cm^{-1} is due to the stretching and deformation vibrations of Bi-O, which belong to Bi_2MoO_6. The absorption peak near 3400 cm^{-1} is due to the vibrations of O-H, which overlaps with the absorption peak of g-C_3N_4. The FT-IR spectra of the composites confirm the preservation of the molecular structure of g-C_3N_4 and the effective dispersion of Bi_2MoO_6 nanoparticles on the surface of g-C_3N_4 nanosheets. The FT-IR results provide additional evidence for the successful preparation of the Bi_2MoO_6/g-C_3N_4 composite photocatalyst and the preservation of the structure and functionality of g-C_3N_4.

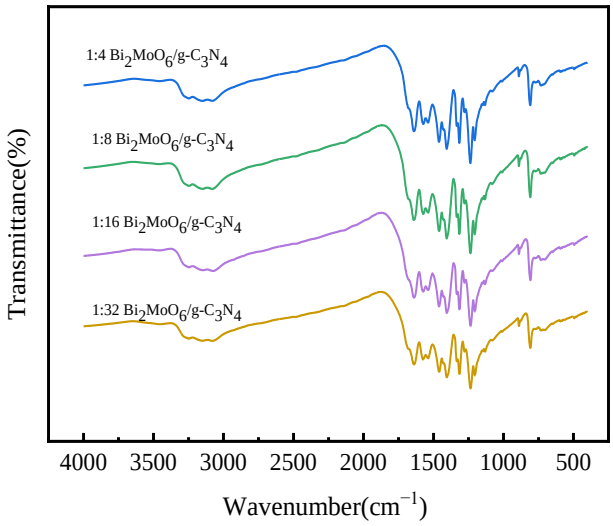

Figure 3. FT-IR spectra of Bi_2MoO_6/g-C_3N_4 with different ratios between Bi_2MoO_6 and g-C_3N_4 prepared in this paper.

PL emission spectra are widely recognized as an effective tool for investigating the migration, transfer, and recombination of photogenerated charge carriers in semiconductors. The PL intensity is strongly correlated with the photodegradation performance of semiconductors. Specifically, a higher PL peak indicates a higher rate of recombination of electron-hole pairs, which in turn leads to a reduced photodegradation activity. Conversely, a lower PL intensity suggests a lower rate of recombination of electron-hole pairs, resulting in an improved photodegradation activity. The main emission peak was centered around 463 nm, as shown in Figure 4. The PL intensities of these samples prepared in this study were ranked in descending order: g-C_3N_4 > Bi_2MoO_6 > 1:32 Bi_2MoO_6/g-C_3N_4. These results confirmed that 1:32 Bi_2MoO_6/g-C_3N_4 exhibits the lowest photogenerated electron-hole recombination rate, which implies superior photodegradation activity.

The photocatalytic activity of a photocatalyst is determined by its ability to absorb and utilize light, which is crucial for photocatalysis. In the case of nanomaterials, their optical absorption properties can be investigated by the UV–vis DRS technique. As shown in Figure 5, all the samples exhibit a certain level of light absorption in the UV range and a response in the visible range, which is mainly determined by the bandgap width of the samples. The absorption edge of the g-C_3N_4 is located at around 438 nm, while that of Bi_2MoO_6 is at around 460 nm. The absorption edge of the 1:32 Bi_2MoO_6/g-C_3N_4 composite is located at around 436 nm in the g-C_3N_4 coupling with Bi_2MoO_6, compared to pure g-C_3N_4 and Bi_2MoO_6. According to the Kubelka–Munk function [60], the indirect band gap energies of the g-C_3N_4, the Bi_2MoO_6 and the 1:32 Bi_2MoO_6/g-C_3N_4 are 2.96 eV, 3.03 eV and 3.00 eV, respectively. These findings imply that the 1:32 Bi_2MoO_6/g-C_3N_4 may

possess superior solar energy utilization and higher photocatalytic activity in contrast to pure g-C_3N_4 and pure Bi_2MoO_6.

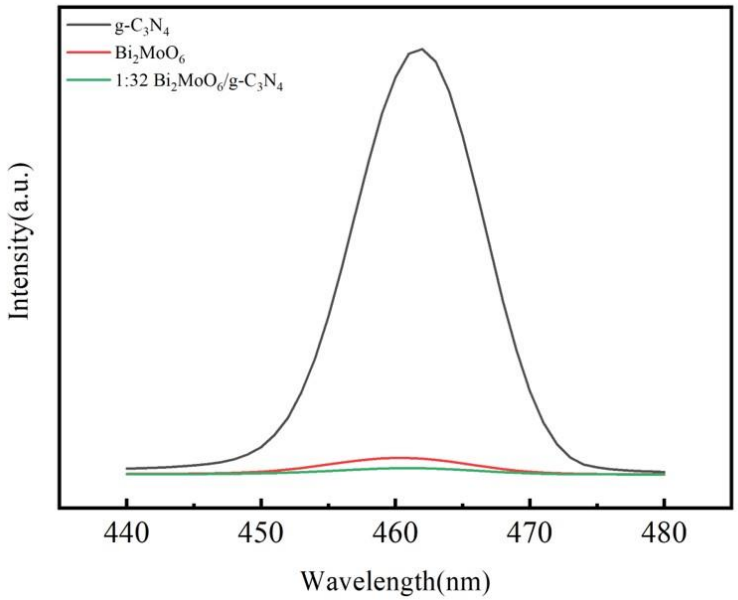

Figure 4. Photoluminescence emission spectra of g-C_3N_4, Bi_2MoO_6 and 1:32 Bi_2MoO_6/g-C_3N_4.

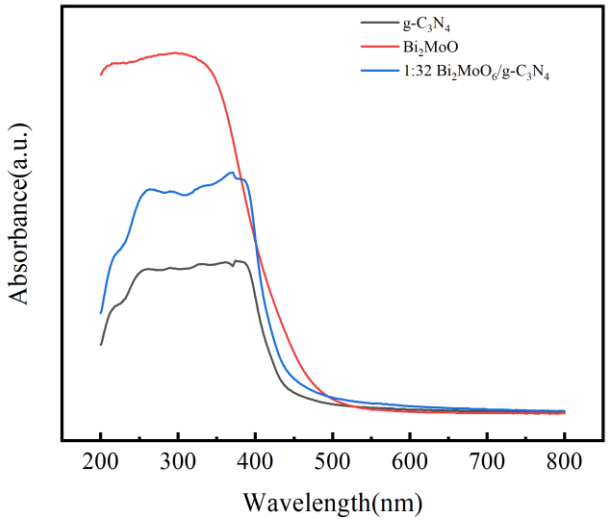

Figure 5. UV–vis spectra a of g-C_3N_4, Bi_2MoO_6 and 1:32 Bi_2MoO_6/g-C_3N_4.

The evaluation of charge carrier separation and transportation capacity during photocatalytic reactions could be conducted through the EIS technique. The semicircles that are apparent in the EIS graphs are mainly attributed to the surface charge transfer resistance of the electrode material. Typically, a reduced radius of the arc in an EIS Nyquist plot corresponds to a decreased electron-hole pair recombination rate, while an increased radius of the arc is indicative of an accelerated rate of recombination. Figure 6 presents the Nyquist plots of the EIS results obtained for pure g-C_3N_4 and 1:32 Bi_2MoO_6/g-C_3N_4. As demonstrated in the figure, the 1:32 Bi_2MoO_6/g-C_3N_4 sample displays a smaller arc radius compared to pure g-C_3N_4, indicating that the presence of Bi_2MoO_6 can improve the separation of electron-hole pairs in g-C_3N_4, consistent with the PL results. In brief, these findings reveal that 1:32 Bi_2MoO_6/g-C_3N_4 may be a highly promising photocatalyst.

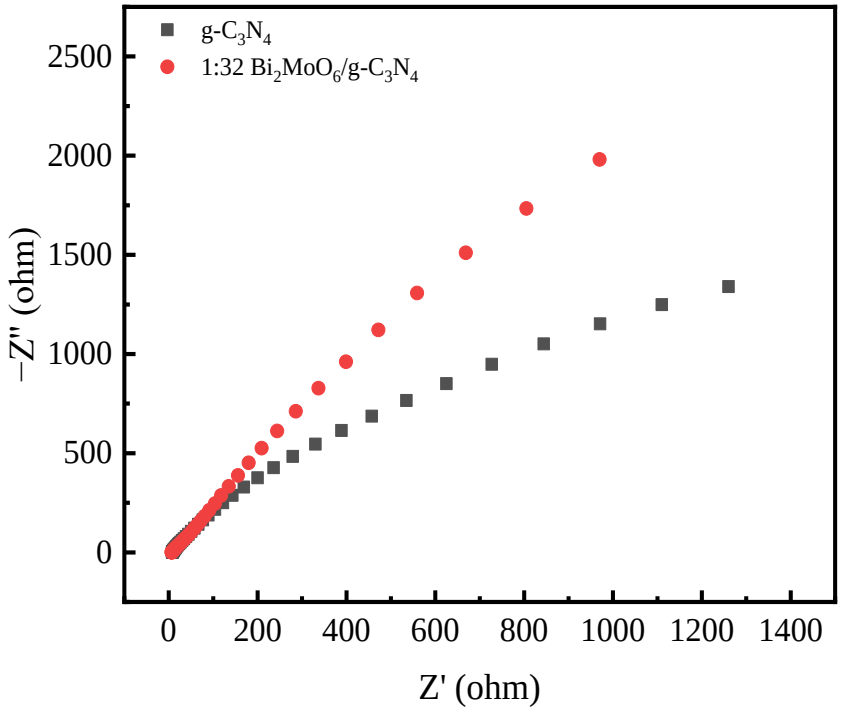

Figure 6. Electrochemical impedance spectra over g-C_3N_4 and 1:32 Bi_2MoO_6/g-C_3N_4 as working electrode.

3.2. Photocatalyst Performance Analysis

Because of SDZ's high stability, it is very difficult to degrade SDZ without the aid of a photocatalyst. Results showed that photocatalysts in the dark condition had limited efficacy in SDZ removal, indicating that SDZ adsorption could be disregarded. After exposing SDZ to visible light for 120 min, it was observed that there was minimal removal efficiency (<5%) for SDZ with photocatalysts in the absence of light. This indicates that the contribution of adsorption by photocatalysts can be disregarded. However, the use of photocatalysts with visible light resulted in significant SDZ degradation. In particular, 1:16 Bi_2MoO_6/g-C_3N_4 and 1:32 Bi_2MoO_6/g-C_3N_4 exhibits a substantially higher rate of SDZ degradation compared to bulk g-C_3N_4 under visible light (Figure 7). The photodegradation rate of SDZ by Bi_2MoO_6/g-C_3N_4 increased as the ratio of Bi_2MoO_6 to g-C_3N_4 increased from 1:4 to 1:32. Interestingly, when the ratio was 1:4 and 1:8, a lower rate of SDZ photodegradation was observed compared to bulk g-C_3N_4, which is in line with the literature [61]. The photocatalytic efficiency of g-C_3N_4, 1:4 Bi_2MoO_6/g-C_3N_4, 1:8 Bi_2MoO_6/g-C_3N_4, 1:16 Bi_2MoO_6/g-C_3N_4, and 1:32 Bi_2MoO_6/g-C_3N_4 was recorded at 83.11%, 80.69%, 81.48%, 86.62%, and 93.88% after 120 min visible light irradiation, respectively. The slopes of the lines in the $\ln(C_0/C_t)$ (C_0, the starting concentration of SDZ and C_t, the concentration of SDZ after being irradiated with visible light irradiation for t minutes) versus visible light irradiation time plot were determined to be the SDZ photocatalytic degradation kinetic constants with Bi_2MoO_6/g-C_3N_4 under visible light irradiation as recorded in Figure 7. It was found that the photocatalytic degradation processes of SDZ by Bi_2MoO_6/g-C_3N_4 fit the first-order kinetics model very well. The photodegradation kinetic constants of g-C_3N_4, 1:4 Bi_2MoO_6/g-C_3N_4, 1:8 Bi_2MoO_6/g-C_3N_4, 1:16 Bi_2MoO_6/g-C_3N_4, and 1:32 Bi_2MoO_6/g-C_3N_4 were 0.01470 min^{-1}, 0.01365 min^{-1}, 0.01437 min^{-1}, 0.01666 min^{-1}, and 0.02461 min^{-1}, respectively. The photocatalytic degradation efficiency of the nanocomposites increases gradually with the further decrease in Bi_2MoO_6 content. It can be attributed to the negative shading effect of over-loading Bi_2MoO_6 on the g-CN, which reduces the active sites of g-CN [62]. It is evident from the experiment that the highest photocatalytic degradation of SDZ was achieved by 1:32 Bi_2MoO_6/g-C_3N_4 under the present experiment. 1:32 Bi_2MoO_6/g-C_3N_4 showed superior photocatalytic activity compared to other photo-

catalysts reported in the literature for the photodegradation of SDZ under visible light irradiation [63–65]. The stability and reusability of 1:32 Bi_2MoO_6/g-C_3N_4 were also examined to provide insight into the practical applications. As shown in Figure 8, a slight reduction in removal efficiency was observed after the fifth experiment, which remained as high as 90%. This slight reduction in removal efficiency may be attributed to some effective sites being plugged during the oxidation process.

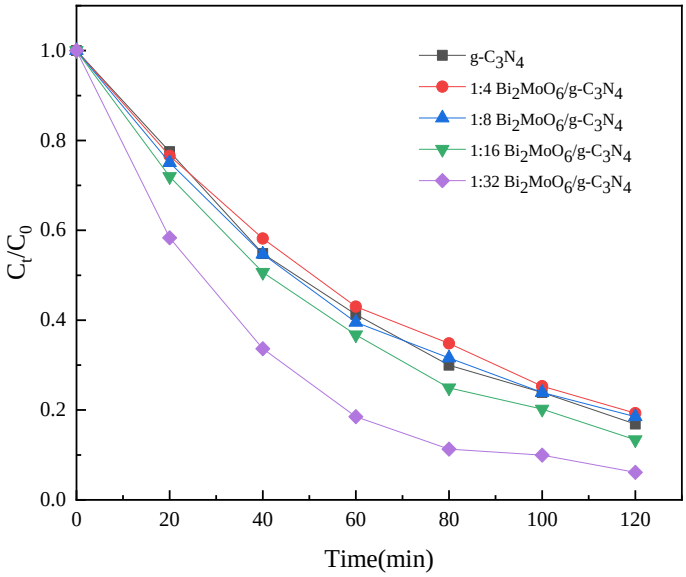

(**a**)

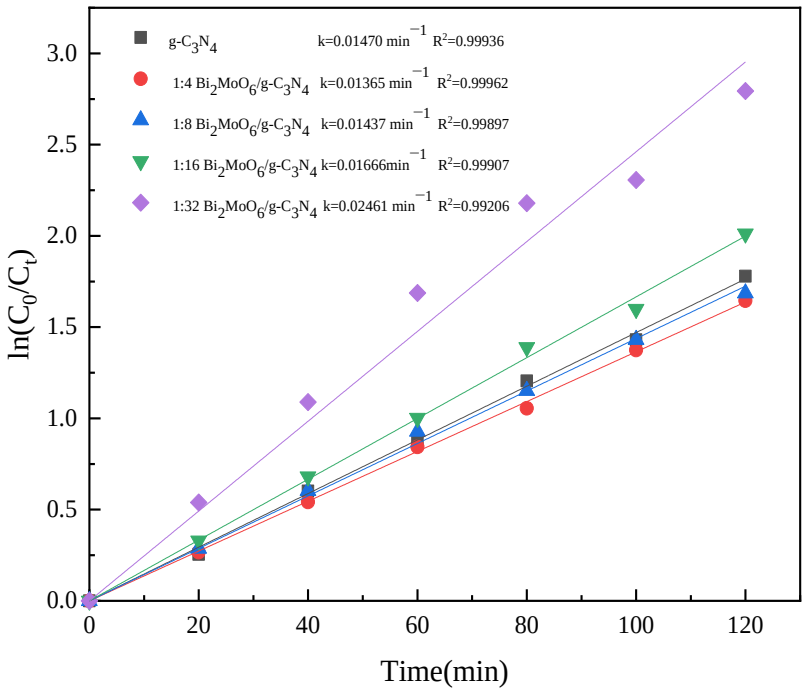

(**b**)

Figure 7. (**a**) Photocatalytic efficiencies of Bi_2MoO_6/g-C_3N_4 with different ratios between Bi_2MoO_6 and g-C_3N_4 for SDZ under visible light irradiation. (**b**) Plots of ln(C_0/C_t) versus irradiation time for SDZ.

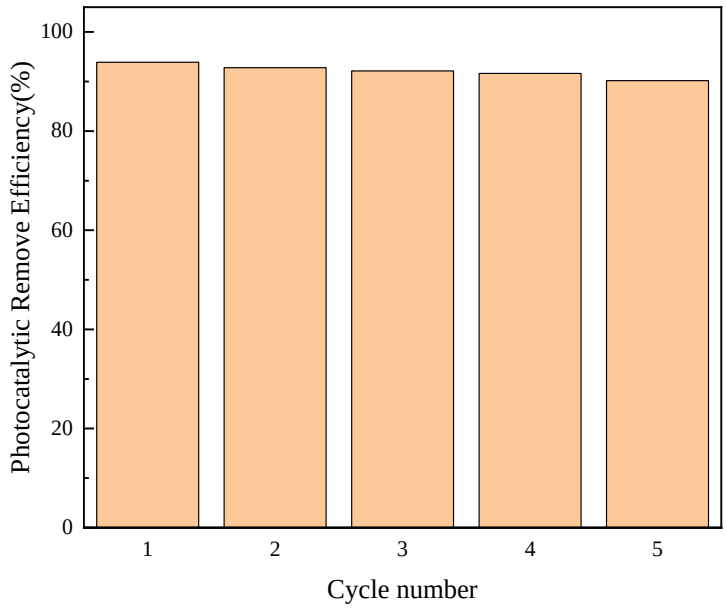

Figure 8. Repeated photodegradation and stability of 1:32 Bi_2MoO_6/g-C_3N_4 for SDZ.

4. Conclusions

In summary, a series of Bi_2MoO_6/g-C_3N_4 composites were successfully prepared via wet-impregnation, and their photocatalytic activity for the degradation of sulfadiazine (SDZ) under visible light irradiation was investigated. The physical and chemical characterizations were investigated using SEM, XRD, FT-IR, DRS, PL, and EIS analysis. The introduction of Bi_2MoO_6 significantly enhanced the visible light responsive photocatalytic activity of the composites. Especially, the 1:32 Bi_2MoO_6/g-C_3N_4 composite exhibits the highest efficiency in degrading SDZ under visible light irradiation with a photocatalytic efficiency of 93.88% after 120 min of visible light irradiation. The results showed that the 1:32 Bi_2MoO_6/g-C_3N_4 composite had the highest efficiency in degrading SDZ under visible light irradiation. This improvement in photocatalytic activity can be attributed to the formation of a heterojunction between Bi_2MoO_6 and g-C_3N_4, which promotes the transfer of photogenerated electron-hole pairs. Furthermore, the stability and reusability of the 1:32 Bi_2MoO_6/g-C_3N_4 composite were also examined, and the results suggest that this composite is stable and reusable, which is promising for its practical applications in wastewater treatment and environmental pollution control. Our study has thus provided valuable insights into the optimization of Bi_2MoO_6/g-C_3N_4 composite ratios for efficient sulfadiazine degradation under visible light irradiation, contributing to the development of novel photocatalysts for the treatment of antibiotic-contaminated wastewater.

Author Contributions: Conceptualization, K.L., M.C. and L.C.; methodology, W.X., S.Z. and Y.H.; software M.C. and W.X.; investigation, M.C., W.X. and S.Z.; resources, K.L. and L.C.; data curation, K.L.; writing—original draft preparation, K.L., M.C. and W.X.; writing—review and editing, K.L. and L.C.; visualization, Y.H.; supervision, K.L. and L.C.; funding acquisition, K.L. and L.C. All authors have read and agreed to the published version of the manuscript.

Funding: This research was funded by National Natural Science Foundation of China (51878316) and Science and Technology Research Planning Project of Jilin Provincial Department of Education (JJKH20220297KJ, JJKH20220279KJ).

Institutional Review Board Statement: Not applicable.

Informed Consent Statement: Not applicable.

Data Availability Statement: Not applicable.

Acknowledgments: All authors thank the editor and anonymous reviewers for their constructive comments and suggestions to improve the quality of this paper.

Conflicts of Interest: The authors declare no conflict of interest. The funders had no role in the design of the study; in the collection, analyses, or interpretation of data; in the writing of the manuscript; or in the decision to publish the results.

References

1. Bargańska, Ż.; Namieśnik, J.; Ślebioda, M. Determination of antibiotic residues in honey. *TrAC Trends Anal. Chem.* **2011**, *30*, 1035–1041. [CrossRef]
2. Ovung, A.; Bhattacharyya, J. Sulfonamide drugs: Structure, antibacterial property, toxicity, and biophysical interactions. *Biophys. Rev.* **2021**, *13*, 259–272. [CrossRef] [PubMed]
3. García-Galán, M.J.; Díaz-Cruz, M.S.; Barceló, D. Identification and determination of metabolites and degradation products of sulfonamide antibiotics. *TrAC Trends Anal. Chem.* **2008**, *27*, 1008–1022. [CrossRef]
4. Feng, G.; Zou, W.; Zhong, Y. Sulfonamides repress cell division in the root apical meristem by inhibiting folates synthesis. *J. Hazard. Mater. Adv.* **2022**, *5*, 100045. [CrossRef]
5. Sköld, O. Sulfonamide resistance: Mechanisms and trends. *Drug Resist. Updates* **2000**, *3*, 155–160. [CrossRef]
6. Kim, H.; Hong, Y.; Park, J.-E.; Sharma, V.K.; Cho, S.-I. Sulfonamides and tetracyclines in livestock wastewater. *Chemosphere* **2013**, *91*, 888–894. [CrossRef] [PubMed]
7. Baran, W.; Adamek, E.; Ziemiańska, J.; Sobczak, A. Effects of the presence of sulfonamides in the environment and their influence on human health. *J. Hazard. Mater.* **2011**, *196*, 1–15. [CrossRef]
8. Su, J.; Fan, J.; Ming, H.; Guo, G.; Fu, Y.; Zhao, X.; Zhao, S.; Chen, Q.; Guan, D.; Jin, Y. The municipal sewage discharge may impact the dissemination of antibiotic-resistant escherichia coli in an urban coastal beach. *Water* **2022**, *14*, 1639. [CrossRef]
9. Kreuzig, R.; Höltge, S.; Brunotte, J.; Berenzen, N.; Wogram, J.; Schulz, R. Test-plot studies on runoff of sulfonamides from manured soils after sprinkler irrigation. *Environ. Toxicol. Chem. Int. J.* **2005**, *24*, 777–781. [CrossRef]
10. Jia, A.; Hu, J.; Wu, X.; Peng, H.; Wu, S.; Dong, Z. Occurrence and source apportionment of sulfonamides and their metabolites in Liaodong Bay and the adjacent Liao River basin, North China. *Environ. Toxicol. Chem.* **2011**, *30*, 1252–1260. [CrossRef]
11. Thai, P.K.; Binh, V.N.; Nhung, P.H.; Nhan, P.T.; Hieu, N.Q.; Dang, N.T.; Tam, N.K.B.; Anh, N.T.K. Occurrence of antibiotic residues and antibiotic-resistant bacteria in effluents of pharmaceutical manufacturers and other sources around Hanoi, Vietnam. *Sci. Total Environ.* **2018**, *645*, 393–400. [CrossRef]
12. García-Galán, M.J.; Blanco, S.G.; Roldán, R.L.; Díaz-Cruz, S.; Barceló, D. Ecotoxicity evaluation and removal of sulfonamides and their acetylated metabolites during conventional wastewater treatment. *Sci. Total Environ.* **2012**, *437*, 403–412. [CrossRef] [PubMed]
13. Liu, Z.; Hu, W.; Zhang, H.; Wang, H.; Sun, P. Enhanced degradation of sulfonamide antibiotics by UV irradiation combined with persulfate. *Processes* **2021**, *9*, 226. [CrossRef]
14. Zhang, T.; Li, B. Occurrence, transformation, and fate of antibiotics in municipal wastewater treatment plants. *Crit. Rev. Environ. Sci. Technol.* **2011**, *41*, 951–998. [CrossRef]
15. Raich-Montiu, J.; Folch, J.; Compañó, R.; Granados, M.; Prat, M. Analysis of trace levels of sulfonamides in surface water and soil samples by liquid chromatography-fluorescence. *J. Chromatogr. A* **2007**, *1172*, 186–193. [CrossRef] [PubMed]
16. Kokoszka, K.; Wilk, J.; Felis, E.; Bajkacz, S. Application of UHPLC-MS/MS method to study occurrence and fate of sulfonamide antibiotics and their transformation products in surface water in highly urbanized areas. *Chemosphere* **2021**, *283*, 131189. [CrossRef] [PubMed]
17. Qin, L.-T.; Pang, X.-R.; Zeng, H.-H.; Liang, Y.-P.; Mo, L.-Y.; Wang, D.-Q.; Dai, J.-F. Ecological and human health risk of sulfonamides in surface water and groundwater of Huixian karst wetland in Guilin, China. *Sci. Total Environ.* **2020**, *708*, 134552. [CrossRef]
18. Gros, M.; Catalán, N.; Mas-Pla, J.; Čelić, M.; Petrović, M.; Farré, M.J. Groundwater antibiotic pollution and its relationship with dissolved organic matter: Identification and environmental implications. *Environ. Pollut.* **2021**, *289*, 117927. [CrossRef]
19. Duan, W.; Cui, H.; Jia, X.; Huang, X. Occurrence and ecotoxicity of sulfonamides in the aquatic environment: A review. *Sci. Total Environ.* **2022**, *820*, 153178. [CrossRef]
20. Spielmeyer, A.; Höper, H.; Hamscher, G. Long-term monitoring of sulfonamide leaching from manure amended soil into groundwater. *Chemosphere* **2017**, *177*, 232–238. [CrossRef]
21. Zhou, J.; Yun, X.; Wang, J.; Li, Q.; Wang, Y. A review on the ecotoxicological effect of sulphonamides on aquatic organisms. *Toxicol. Rep.* **2022**, *9*, 534–540. [CrossRef]
22. Xu, D.; Xie, Y.; Li, J. Toxic effects and molecular mechanisms of sulfamethoxazole on Scenedesmus obliquus. *Ecotoxicol. Environ. Saf.* **2022**, *232*, 113258. [CrossRef] [PubMed]
23. Chen, S.; Zhang, W.; Li, J.; Yuan, M.; Zhang, J.; Xu, F.; Xu, H.; Zheng, X.; Wang, L. Ecotoxicological effects of sulfonamides and fluoroquinolones and their removal by a green alga (*Chlorella vulgaris*) and a cyanobacterium (*Chrysosporum ovalisporum*). *Environ. Pollut.* **2020**, *263*, 114554. [CrossRef] [PubMed]
24. Iftikhar, N.; Konig, I.; English, C.; Ivantsova, E.; Souders, C.L.; Hashmi, I.; Martyniuk, C.J. Sulfamethoxazole (SMX) Alters Immune and Apoptotic Endpoints in Developing Zebrafish (*Danio rerio*). *Toxics* **2023**, *11*, 178. [CrossRef] [PubMed]

25. Hu, F.; Dong, F.; Yin, L.; Wang, H.; Zheng, M.; Fu, S.; Zhang, W. Effects of sulfamethoxazole on the growth, oxidative stress and inflammatory response in the liver of juvenile Nile tilapia (*Oreochromis niloticus*). *Aquaculture* **2021**, *543*, 736935. [CrossRef]
26. Gao, P.; Munir, M.; Xagoraraki, I. Correlation of tetracycline and sulfonamide antibiotics with corresponding resistance genes and resistant bacteria in a conventional municipal wastewater treatment plant. *Sci. Total Environ.* **2012**, *421*, 173–183. [CrossRef]
27. Sabri, N.A.; Schmitt, H.; Van der Zaan, B.; Gerritsen, H.W.; Zuidema, T.; Rijnaarts, H.H.M.; Langenhoff, A.A.M. Prevalence of antibiotics and antibiotic resistance genes in a wastewater effluent-receiving river in the Netherlands. *J. Environ. Chem. Eng.* **2020**, *8*, 102245. [CrossRef]
28. Cuerda-Correa, E.M.; Alexandre-Franco, M.F.; Fernández-González, C. Advanced oxidation processes for the removal of antibiotics from water. An overview. *Water* **2019**, *12*, 102. [CrossRef]
29. Mahdi, M.H.; Mohammed, T.J.; Al-Najar, J.A. Advanced Oxidation Processes (AOPs) for treatment of antibiotics in wastewater: A review. *IOP Conf. Ser. Earth Environ. Sci.* **2021**, *779*, 012109. [CrossRef]
30. Jiang, Y.; Ran, J.; Mao, K.; Yang, X.; Zhong, L.; Yang, C.; Feng, X.; Zhang, H. Recent progress in Fenton/Fenton-like reactions for the removal of antibiotics in aqueous environments. *Ecotoxicol. Environ. Saf.* **2022**, *236*, 113464. [CrossRef]
31. Foroughi, M.; Khiadani, M.; Kakhki, S.; Kholghi, V.; Naderi, K.; Yektay, S. Effect of ozonation-based disinfection methods on the removal of antibiotic resistant bacteria and resistance genes (ARB/ARGs) in water and wastewater treatment: A systematic review. *Sci. Total Environ.* **2022**, *811*, 151404. [CrossRef]
32. Santos, L.V.D.; Meireles, A.M.; Lange, L.C. Degradation of antibiotics norfloxacin by Fenton, UV and UV/H_2O_2. *J. Environ. Manag.* **2015**, *154*, 8–12. [CrossRef] [PubMed]
33. Iakovides, I.C.; Michael-Kordatou, I.; Moreira, N.F.F.; Ribeiro, A.R.; Fernandes, T.; Pereira, M.F.R.; Nunes, O.C.; Manaia, C.M.; Silva, A.M.T.; Fatta-Kassinos, D. Continuous ozonation of urban wastewater: Removal of antibiotics, antibiotic-resistant Escherichia coli and antibiotic resistance genes and phytotoxicity. *Water Res.* **2019**, *159*, 333–347. [CrossRef] [PubMed]
34. Heidari, Z.; Pelalak, R.; Malekshah, R.E.; Pishnamazi, M.; Rezakazemi, M.; Aminabhavi, T.M.; Shirazian, S. A new insight into catalytic ozonation of sulfasalazine antibiotic by plasma-treated limonite nanostructures: Experimental, modeling and mechanism. *Chem. Eng. J.* **2022**, *428*, 131230. [CrossRef]
35. Tang, J.; Zhang, C.; Shi, X.; Sun, J.; Cunningham, J.A. Municipal wastewater treatment plants coupled with electrochemical, biological and bio-electrochemical technologies: Opportunities and challenge toward energy self-sufficiency. *J. Environ. Manag.* **2019**, *234*, 396–403. [CrossRef]
36. He, T.; Zhao, H.; Liu, Y.; Zhao, C.; Wang, L.; Wang, H.; Zhao, Y.; Wang, H. Facile fabrication of superhydrophobic Titanium dioxide-composited cotton fabrics to realize oil-water separation with efficiently photocatalytic degradation for water-soluble pollutants. *Colloids Surf. A Physicochem. Eng. Aspects* **2020**, *585*, 124080. [CrossRef]
37. Pirilä, M.; Saouabe, M.; Ojala, S.; Rathnayake, B.; Drault, F.; Valtanen, A.; Huuhtanen, M.; Brahmi, R.; Keiski, R.L. Photocatalytic degradation of organic pollutants in wastewater. *Top. Catal.* **2015**, *58*, 1085–1099. [CrossRef]
38. Sinar Mashuri, S.I.; Ibrahim, M.L.; Kasim, M.F.; Mastuli, M.S.; Rashid, U.; Abdullah, A.H.; Islam, A.; Asikin Mijan, N.; Tan, Y.H.; Mansir, N. Photocatalysis for organic wastewater treatment: From the basis to current challenges for society. *Catalysts* **2020**, *10*, 1260. [CrossRef]
39. Natarajan, S.; Bajaj, H.C.; Tayade, R.J. Recent advances based on the synergetic effect of adsorption for removal of dyes from waste water using photocatalytic process. *J. Environ. Sci.* **2018**, *65*, 201–222. [CrossRef]
40. Kositzi, M.; Poulios, I.; Malato, S.; Caceres, J.; Campos, A. Solar photocatalytic treatment of synthetic municipal wastewater. *Water Res.* **2004**, *38*, 1147–1154. [CrossRef] [PubMed]
41. Yahya, N.; Aziz, F.; Jamaludin, N.; Mutalib, M.; Ismail, A.; Salleh, W.; Jaafar, J.; Yusof, N.; Ludin, N. A review of integrated photocatalyst adsorbents for wastewater treatment. *J. Environ. Chem. Eng.* **2018**, *6*, 7411–7425. [CrossRef]
42. Lee, K.M.; Lai, C.W.; Ngai, K.S.; Juan, J.C. Recent developments of zinc oxide based photocatalyst in water treatment technology: A review. *Water Res.* **2016**, *88*, 428–448. [CrossRef] [PubMed]
43. Malathi, A.; Madhavan, J.; Ashokkumar, M.; Arunachalam, P. A review on BiVO4 photocatalyst: Activity enhancement methods for solar photocatalytic applications. *Appl. Catal. A Gen.* **2018**, *555*, 47–74.
44. Pekakis, P.A.; Xekoukoulotakis, N.P.; Mantzavinos, D. Treatment of textile dyehouse wastewater by TiO_2 photocatalysis. *Water Res.* **2006**, *40*, 1276–1286. [CrossRef]
45. Tan, M.; Qiu, G.; Ting, Y.-P. Effects of ZnO nanoparticles on wastewater treatment and their removal behavior in a membrane bioreactor. *Bioresour. Technol.* **2015**, *185*, 125–133. [CrossRef] [PubMed]
46. Yu, C.; Chen, X.; Li, N.; Zhang, Y.; Li, S.; Chen, J.; Yao, L.; Lin, K.; Lai, Y.; Deng, X. Ag_3PO_4-based photocatalysts and their application in organic-polluted wastewater treatment. *Environ. Sci. Pollut. Res.* **2022**, *29*, 18423–18439. [CrossRef]
47. Tao, Q.; Bi, J.; Huang, X.; Wei, R.; Wang, T.; Zhou, Y.; Hao, H. Fabrication, application, optimization and working mechanism of Fe2O3 and its composites for contaminants elimination from wastewater. *Chemosphere* **2021**, *263*, 127889. [CrossRef]
48. Mandal, R.K.; Pradhan, S.K. Superior photocatalytic performance of mechanosynthesized Bi_2O_3–Bi_2WO_6 nanocomposite in wastewater treatment. *Solid State Sci.* **2021**, *115*, 06587. [CrossRef]
49. Chen, Q.; Li, J.; Li, X.; Huang, K.; Zhou, B.; Cai, W.; Shangguan, W. Visible-light responsive photocatalytic fuel cell based on WO_3/W photoanode and Cu_2O/Cu photocathode for simultaneous wastewater treatment and electricity generation. *Environ. Sci. Technol.* **2012**, *46*, 11451–11458. [CrossRef]

50. Dong, H.; Guo, X.T.; Yang, C.; Ouyang, Z.Z. Synthesis of g-C_3N_4 by different precursors under burning explosion effect and its photocatalytic degradation for tylosin. *Appl. Catal. B-Environ.* **2018**, *230*, 65–76. [CrossRef]
51. Song, Y.L.; Tian, J.Y.; Gao, S.S.; Shao, P.H.; Qi, J.Y.; Cui, F.Y. Photodegradation of sulfonamides by g-C_3N_4 under visible light irradiation: Effectiveness, mechanism and pathways. *Appl. Catal. B-Environ.* **2017**, *210*, 88–96. [CrossRef]
52. Zhou, P.; Meng, X.L.; Sun, T.H. Facile fabrication of In_2O_3/S-doped g-C_3N_4 heterojunction hybrids for enhanced visible-light photocatalytic hydrogen evolution. *Mater. Lett.* **2020**, *261*, 127159. [CrossRef]
53. Nakata, K.; Fujishima, A. TiO_2 photocatalysis: Design and applications. *J. Photochem. Photobiol. C Photochem. Rev.* **2012**, *13*, 169–189. [CrossRef]
54. Jiang, G.D.; Yang, X.X.; Wu, Y.; Li, Z.W.; Han, Y.H.; Shen, X.D. A study of spherical TiO_2/g-C_3N_4 photocatalyst: Morphology, chemical composition and photocatalytic performance in visible light. *Mol. Catal.* **2017**, *432*, 232–241. [CrossRef]
55. Song, G.; Xin, F.; Yin, X. Photocatalytic reduction of carbon dioxide over $ZnFe_2O_4$/TiO_2 nanobelts heterostructure in cyclohexanol. *J. Colloid Interface Sci.* **2015**, *442*, 60–66. [CrossRef]
56. Solakidou, M.; Giannakas, A.; Georgiou, Y.; Boukos, N.; Louloudi, M.; Deligiannakis, Y. Efficient photocatalytic water-splitting performance by ternary CdS/Pt-N-TiO_2 and CdS/Pt-N, F-TiO_2: Interplay between CdS photo corrosion and TiO_2-dopping. *Appl. Catal. B Environ.* **2019**, *254*, 194–205. [CrossRef]
57. Fu, K.; Pan, Y.S.; Ding, C.; Shi, J.; Deng, H.P. Photocatalytic degradation of naproxen by Bi_2MoO_6/g-C_3N_4 heterojunction photocatalyst under visible light: Mechanisms, degradation pathway, and DFT calculation. *J. Photochem. Photobiol. A Chem.* **2021**, *412*, 113235. [CrossRef]
58. Kasinathan, M.; Thiripuranthagan, S.; Sivakumar, A. Fabrication of 3D/2D Bi_2MoO_6/g-C_3N_4 heterostructure with enhanced photocatalytic behavior in the degradation of harmful organics. *Emergent Mat.* **2021**, *4*, 1363–1376. [CrossRef]
59. Yang, J.-F.; Ying, G.-G.; Yang, L.-H.; Zhao, J.-L.; Liu, F.; Tao, R.; Yu, Z.-Q.; Peng, P. Degradation behavior of sulfadiazine in soils under different conditions. *J. Environ. Sci. Health Part B* **2009**, *44*, 241–248. [CrossRef]
60. Landi, S., Jr.; Segundo, I.R.; Freitas, E.; Vasilevskiy, M.; Carneiro, J.; Tavares, C.J. Use and misuse of the Kubelka-Munk function to obtain the band gap energy from diffuse reflectance measurements. *Solid State Commun.* **2022**, *341*, 114573. [CrossRef]
61. Li, H.P.; Liu, J.Y.; Hou, W.G.; Du, N.; Zhang, R.J.; Tao, X.T. Synthesis and characterization of g-C_3N_4/Bi_2MoO_6 heterojunctions with enhanced visible light photocatalytic activity. *Appl. Catal. B-Environ.* **2014**, *160*, 89–97. [CrossRef]
62. Preeyanghaa, M.; Dhileepan, M.D.; Madhavan, J.; Neppolian, B. Revealing the charge transfer mechanism in magnetically recyclable ternary g-C_3N_4/BiOBr/Fe_3O_4 nanocomposite for efficient photocatalytic degradation of tetracycline antibiotics. *Chemosphere* **2022**, *303*, 135070. [CrossRef] [PubMed]
63. Liu, X.H.; Liu, Y.; Lu, S.Y.; Guo, W.; Xi, B.D. Performance and mechanism into TiO_2/Zeolite composites for sulfadiazine adsorption and photodegradation. *Chem. Eng. J.* **2018**, *350*, 131–147. [CrossRef]
64. Naciri, Y.; Bouddouch, A.; Bakiz, B.; Taoufyq, A.; Ezahri, M.; Benlhachemi, A. Photocatalytic degradation of sulfadiazine by Zn-$_3(PO_4)_2$/$BiPO_4$ composites upon UV light irradiation. *Mater. Today-Proc.* **2020**, *22*, 48–51. [CrossRef]
65. Li, D.P.; Zhang, N.; Yuan, R.F.; Chen, H.L.; Wang, F.; Zhou, B.H. Effect of wavelengths on photocatalytic oxidation mechanism of sulfadiazine and sulfamethoxazole in the presence of TiO_2. *J. Environ. Chem. Eng.* **2021**, *9*, 106243. [CrossRef]